Nano Research 2018, 11(3): 1599–1611
https://doi.org/10.1007/s12274-017-1775-0
Research Article
ISSN 1998-0124
CN 11-5974/O4

A systematic theoretical study on FeO_x-supported single-atom catalysts: M_1/FeO_x for CO oxidation

Jinxia Liang[1,2,3], Qi Yu[2], Xiaofeng Yang[4] (✉), Tao Zhang[4], and Jun Li[3] (✉)

[1] *Guizhou Provincial Key Laboratory of Computational Nano-Material Science, Guizhou Synergetic Innovation Center of Scientific Big Data for Advanced Manufacturing Technology, Guizhou Education University, Guiyang 550018, China*
[2] *Shaanxi Key Laboratory of Catalysis, Shaanxi University of Technology, Hanzhong 723000, China*
[3] *Department of Chemistry and Key Laboratory of Organic Optoelectronics & Molecular Engineering of Ministry of Education, Tsinghua University, Beijing 100084, China*
[4] *State Key Laboratory of Catalysis, Dalian Institute of Chemical Physics, Chinese Academy of Sciences, Dalian 116023, China*

Received: 4 July 2017
Revised: 22 July 2017
Accepted: 24 July 2017

KEYWORDS
single-atom catalyst,
M_1/FeO_x,
density functional theory,
heterogeneous catalysis

ABSTRACT

A single-atom catalyst (SAC) that was first proposed by us in 2011 has aroused significant recent interest. Among the various SACs, FeO_x-based ones including Pt_1/FeO_x, Ir_1/FeO_x, Au_1/FeO_x, Ni_1/FeO_x, and Fe_1/FeO_x have been investigated either experimentally or theoretically for CO oxidation. However, a systematic study of FeO_x-based SACs has not been conducted. For a comprehensive understanding of FeO_x-supported single-metal-atom catalysts, extensive density functional theory calculations were carried out on the activities and catalytic mechanisms of SACs with the 3d, 4d, and 5d metals of group VIII to IB, i.e., M_1/FeO_x (M = Fe, Co, Ni, Cu; Ru, Rh, Pd, Ag; Os, Ir, Pt, Au) for CO oxidation. Remarkably, a new noble metal SAC, Pd_1/FeO_x, with high activity in CO oxidation was found and is predicted to be even better than the previously reported Pt_1/FeO_x and Ni_1/FeO_x. In comparison, other M_1/FeO_x SACs (M = Fe, Co, Cu; Ru, Rh, Ag; Os, Ir, Au) showed only low activities in CO oxidation. Moreover, the adsorption strength of CO on the single-atom active sites was found to be the key in determining the catalytic activity of these SACs for CO oxidation, because it governs the recoverability of oxygen vacancies on their surfaces in the formation of a second CO_2 during CO oxidation. Our systematic studies of FeO_x-supported SACs will help in understanding the fundamental mechanisms of the interactions between singly dispersed surface metal atoms and FeO_x substrate and in designing highly active FeO_x-supported SACs.

1 Introduction

Oxide-supported metals are used extensively as catalysts in the chemical industry. It is well known that metal size [1–11] and substrate type [6, 12–14] are important factors that determine the performances of

Address correspondence to Xiaofeng Yang, yangxf2003@dicp.ac.cn; Jun Li, junli@tsinghua.edu.cn

such catalysts. Notably, reducing the size of metal particles to nano-/subnanoclusters or even to single atoms can greatly enhance the activity of a metal species, although this lowers the intrinsic thermodynamic stabilities of these species owing to high surface energies. However, with appropriate supports or ligands, the single atoms and small-sized clusters can be stabilized via covalent metal-support interactions (CMSIs) in addition to ionic interactions.

Our first realization of a practical single-atom catalyst (SAC) [1] demonstrated that Pt particles or clusters can be reduced in size to monodispersed single-atom Pt_1 active sites on an FeO_x support. Interestingly, this Pt_1/FeO_x SAC was found to be highly efficient for CO oxidation reactions. Our density functional theory (DFT) calculations showed that the high catalytic activity was correlated with the partially vacant 5d orbitals of the positively charged, high-valent Pt atoms, which reduce the likelihood of CO poisoning and facilitate the adsorption and activation of dioxygen.

Since its proposal, significant progress has been made on the SAC concept over the past several years. SACs with different metals or substrates have been found to exhibit excellent catalytic performances and stabilities in various chemical reactions [4, 5, 8, 15–55]. FeO_x-supported SACs now include not only Pt_1/FeO_x but also Ir_1/FeO_x [8, 56], Au_1/FeO_x [57, 58], Ni_1/FeO_x [59], and Fe_1/FeO_x [26]. These SACs also contain well-defined single metal atoms on iron oxide, but the catalytic behavior in CO oxidation varies with the metal used. For example, experimental results revealed that the Ir_1/FeO_x catalyst showed lower activity for CO oxidation than Pt_1/FeO_x [56]. Meanwhile, a theoretical investigation predicted that the non-noble SAC Ni_1/FeO_x can show high catalytic activity for CO oxidation at room temperature, but the non-doped Fe_1/FeO_x substrate is nearly inert [26]. Using a similar theoretical model to that reported in Ref. [1], Li et al. studied the catalytic properties and mechanisms of several M_1/FeO_x SACs (M = Rh, Pd, Co, Cu, Ru, and Ti) for CO oxidation and the adsorption of CO and O_2 on Au_1/FeO_x [60]. However, a comprehensive fundamental understanding of the stability and activity trends in the periodic table as well as the catalytic mechanisms of the FeO_x-based SACs with 3d, 4d, and 5d metals from groups VIII to IB for CO oxidation is still necessary. Among the various efforts to elucidate the nature of the stability of SACs, the recent work by Liu et al. is of particular importance; they studied the stabilities of SACs on various supports and formed a chemical potential-based model for the design of highly stable SACs on oxide surfaces [28, 61]. Such a study can enable systematic screening of FeO_x-based SACs so as to guide future experiments.

CO oxidation has been investigated extensively and is important for environmental protection, exhaust purification for motor vehicles, gas purification for closed-cycle CO_2 lasers, CO detectors, and other applications [7, 62–68]. CO oxidation is also an elementary step in the water-gas shift (WGS) reaction [8, 69, 70]. Moreover, preferential oxidation of CO in H_2 (PROX) is also a key step in removing CO from reforming gas in fuel cell applications [71]. In the past few decades, a number of oxide-supported transition metals (Pt, Au, Ir, Pd, Ni, etc.) [1, 5, 72–74] have been identified as active catalysts for CO oxidation.

In order to systematically determine the activities and catalytic mechanism of M_1/FeO_x SACs in CO oxidation and elucidate the nature of the binding of single M_1 3d, 4d, and 5d atoms from groups VIII to IB (M = Fe, Co, Ni, Cu; Ru, Rh, Pd, Ag; Os, Ir, Pt, Au) to an FeO_x support in these M_1/FeO_x SACs, we conducted extensive theoretical investigations using relativistic DFT on the possible catalytic reaction mechanisms with some M_1/FeO_x (M = Co, Cu; Ru, Rh, Pd, Ag; Os) SACs and the electronic properties of the reactants, transition states, and intermediate products. Meanwhile, Bader charge analysis was conducted and the adsorption energies of CO on the surfaces of the M_1/FeO_x SACs and the density of states (DOS) were calculated to evaluate the performances of these M_1/FeO_x catalysts in CO oxidation. These results together with previously published results [1, 26, 57, 59] enable the systematic evaluation of all M_1/FeO_x catalysts with metals from group VIII to IB. Based on these studies, a new SAC, Pd_1/FeO_x, is predicted to show promising catalytic activity for CO oxidation at room temperature. Meanwhile, the adsorption strength of CO on the single-atom active sites, identified as a catalytic descriptor, was found to be the key factor in the catalytic activity for CO oxidation in these SACs because it governs the recoverability of oxygen vacancies on

their surfaces in the formation of a second CO_2. These results can help in understanding the fundamental mechanisms of FeO_x-based SACs in CO oxidation and designing highly active FeO_x-supported SACs for practical applications involving CO oxidation.

2 Computational details

As in our previous work [1], the (0001) surfaces of α-Fe_2O_3 were represented by a periodic slab model constructed using bulk cell dimensions: $a = b = 5.04$ Å and $c = 13.72$ Å. Since α-Fe_2O_3 is antiferromagnetic and has an atomic magnetic moment on the iron atoms, we used the primitive rhombohedral unit cell of Fe_2O_3 with the magnetic configuration (+ − − +) to build the surface slab; this was previously shown to be the most energetically favored magnetic configuration for α-Fe_2O_3 [75]. A vacuum distance 12 Å wide in the direction perpendicular to the surface was applied to eliminate the interaction between layered nanostructures in the adjacent cells. Since the relaxations of the Fe_2O_3 surfaces are usually very large [1, 76], we chose slabs containing 12 layers of Fe atoms and seven atomic layers of O_3 (see below) to model the O_3-terminated surfaces [1]. The ten top-layer slabs of the surface were allowed to relax while the other layers beneath the surface were frozen during the geometry optimizations. On the basis of previous studies [1, 16], the relatively favorable O_3-terminated surface of Fe_2O_3(0001) was selected to stabilize the M_1 (M = Co, Ni, Cu; Ru, Rh, Pd, Ag; Os) single atoms; each M_1 atom was coordinated to three surface oxygen atoms (i.e., the O_3 atoms), with the third-layer Fe atoms lying below the M_1 atoms. The single M_1 atoms can be viewed as being in this location owing to replacing the surface Fe atoms on the O_3-terminated surface.

The theoretical calculations were performed at the DFT level using the Vienna *ab initio* simulation package (VASP) [77, 78]. The core and valence electrons were represented by using the projector augmented wave (PAW) [79] method and plane-wave basis functions with a kinetic energy cut-off of 400 eV [1]. Inasmuch as heavier M_1 transition metals have significant relativistic effects, the mass-velocity and Darwin relativistic effects were included through the PAW potentials, without accounting for the possible spin-orbit effects. The generalized gradient approximation (GGA) with the Perdew–Burke–Ernzerhof (PBE) [80] exchange-correlation functional was used in the calculations. A 3 × 3 × 1 Monkhorst–Pack grid was used to sample the surface Brillouin zone [1]. Ground-state atomic geometries were obtained by minimizing the forces on the atoms below 0.02 eV/Å. Because of the strong d-electron correlation effects for Fe and other 3d metals, the calculations were carried out with the DFT+U method using the formalism suggested by Liechtenstein and Dudarev et al. [81]. The parameters were set to $U = 4$ eV and $J = 1$ eV based on a previous study [1]. The transition states were obtained by relaxing the force below 0.05 eV/Å using the dimer method [82].

3 Results and discussion

3.1 Catalytic cycle of CO oxidation on M_1/FeO_x catalyst

In order to determine the relative catalytic performances of the 3d, 4d, and 5d metals from groups VIII to IB supported on α-Fe_2O_3, we used our previous geometric model [1, 26, 56, 57] with an oxygen vacancy (O_{vac}) on the (0001) surface of α-Fe_2O_3 to investigate the catalytic mechanism for CO oxidation on M_1/FeO_x (M = Co, Cu; Ru, Rh, Pd, Ag; Os), with our previous results from Pt_1/FeO_x [1], Ir_1/FeO_x [56], Au_1/FeO_x [57], Ni_1/FeO_x [59], and Fe_1/FeO_x [26] as references. The local site of the geometric model of M_1/FeO_x is shown in Scheme 1.

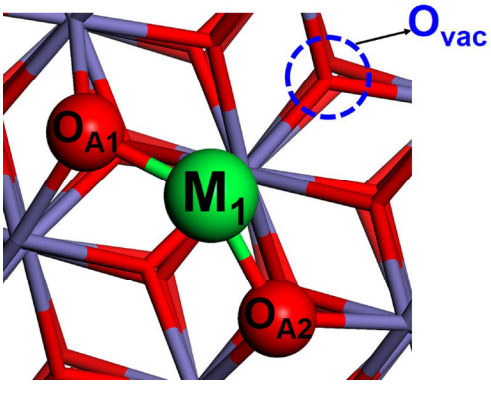

Scheme 1 Local SAC site of the geometric model of M_1/FeO_x. O_{A1} and O_{A2} represent the surface lattice O atoms of the support, and O_{vac} is located at the upper-right corner.

As indicated in step i of Fig. 1, the optimized M_1–O_{A1} and M_1–O_{A2} bond lengths (see Scheme 1) were 1.78 and 1.77 Å for Fe_1/FeO_x, 1.74 and 1.73 Å for Co_1/FeO_x, 1.87 and 1.85 Å for Ru_1/FeO_x, 1.91 and 1.89 Å for Rh_1/FeO_x, 1.79 and 1.79 Å for Os_1/FeO_x, and 1.85 and 1.83 Å for Ir_1/FeO_x [56], respectively (see Table S1 in the Electronic Supplementary Material (ESM)). These results show that different single atoms have distinctive binding geometries, thus providing opportunities to tune catalytic properties by adjusting the heterogeneously supported surface metal atoms.

3.1.1 *Formation of the first CO_2 associated with oxygen dissociation*

Like that on Ni_1/FeO_x, the formation of the first CO_2 associated with oxygen dissociation was also found to occur on other M_1/FeO_x (M = Fe, Co; Ru, Rh; Os, Ir) SACs. The energy profile is shown in Fig. 1, while the schematic structures at each reaction step shown beneath the reaction pathways and the optimized partial bond lengths are displayed in Table S1 (in the ESM).

On these surfaces, O_2 dissociates with one oxygen atom (O_B) vertically adsorbed on the single M_1 atoms (M = Fe, Co; Ru, Rh; Os, Ir) and the other (O_C) in the O_{vac} site (step ii_{dis}). The O_B–O_C bond lengths were 2.70, 2.82, 3.14, and 3.18 Å on the M_1/FeO_x SACs when M was Fe, Co, Rh, and Ir, respectively. Meanwhile, the adsorption energies of dissociated O_2 (3.75, 3.11, 3.54, and 3.85 eV) were much higher than those of adsorbed O_2 (2.14, 2.02, 2.23, and 1.20 eV) on the M_1/FeO_x SACs (M = Fe, Co; Rh; Ir, see Table S2 in the ESM), indicating that an adsorbed oxygen molecule ($O_{2,ad}$) is easier to dissociate on these single M_1 atoms and O_{vac} in M_1/FeO_x. Moreover, on the surfaces of the Ru_1/FeO_x and Os_1/FeO_x SACs, only the dissociative state of O_2 can be obtained, suggesting that such dissociation occurs spontaneously, and the calculated adsorption energies of dissociated O_2 were as high as 4.52 and 5.02 eV, respectively, consistent with the value from a previous report on O_2 adsorption on Ru_1/FeO_x (4.48 eV) [61].

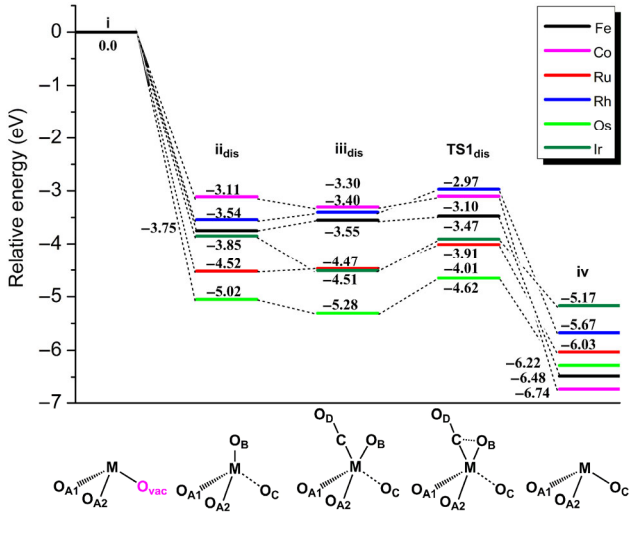

Figure 1 Proposed reaction pathway of the formation of the first CO_2 associated with oxygen dissociation on M_1/FeO_x (M = Fe, Co; Ru, Rh; Os, Ir) catalysts, starting from the surface with the O_{vac}. Here, the O_B and O_C atoms are derived from the dissociation of an oxygen gas molecule, while the O_D atom comes from CO gas.

In step iii_{dis}, the first CO is adsorbed on the single M_1 atoms via the Langmuir–Hinshelwood (L–H) mechanism [84, 85], with binding energies of −0.20, 0.19, −0.05, −0.14, 0.26, and 0.66 eV (negative values here represent as endothermic adsorption) when M was Fe, Co, Ru, Rh, Os, and Ir, respectively. As O_B approached the carbon atom of co-adsorbed CO, the distances between them (C–O_B) decreased from 2.36 to 1.94 Å (Fe), 2.35 to 1.90 Å (Co), 2.54 to 1.75 Å (Ru), 2.49 to 1.79 Å (Rh), 2.56 to 1.70 Å (Os), and 2.49 to 1.71 Å (Ir), leading to low activation barriers of 0.08, 0.20, 0.46, 0.43, 0.66, and 0.60 eV, to form the first transition states ($TS1_{dis}$) for $CO_{ad} + O_B \rightarrow CO_2$ on M_1/FeO_x when M was Fe, Co, Ru, Rh, Os, and Ir, respectively. Obviously, these activation barriers of the first CO oxidation are low enough for the reaction to occur at a low temperature. When the first CO_2 molecules are released from the surfaces of these M_1/FeO_x catalysts, the remaining O_C atom fills the surface vacancy to generate a stoichiometric hematite surface (step iv).

According to our previous study on the Ir_1/FeO_x SAC, the Eley–Rideal (E–R) mechanism cannot be excluded *a priori* owing to the possible reactivity of the vertically adsorbed O_B atom towards gaseous CO. Therefore, the E–R mechanism for the formation of CO_2 was also considered on the M_1/FeO_x (M = Fe, Co; Ru, Rh; Os) SACs. The calculated reaction pathway and the corresponding schematic structures, including the initial reactant (R), transition state (TS), and final product (P), are shown in Fig. S1 in the ESM, while the selected distances of atoms are displayed in Table S3

in the ESM. Figure S1 and Table S3 in the ESM show that, for the initial reactants (R), the interactions between CO molecules in the gas and the dissociated O_B atoms on the single Fe, Co, Ru, Rh, and Os atoms are rather weak; the optimized distances between carbon and the vertically adsorbed O_B (C–O_B) were 3.33, 2.96, 3.87, 3.13, and 3.23 Å, respectively. In the transition states (TS), the C–O_B distances decreased to 1.83, 1.86, 1.58, 1.72, and 1.47 Å, respectively, and the bond lengths between the single M_1 atoms and the dissociated O_B atom (M_1–O_B) increased from 1.59 to 1.66 Å (for M = Fe), 1.60 to 1.64 Å (Co), 1.70 to 1.80 Å (Ru), 1.60 to 1.64 Å (Rh), and 1.71 to 1.87 Å (Os), indicating the formation of CO_2 molecules. After the reaction passes $TS1_{dis}$, CO_2 molecules are generated and easily desorbed from the surfaces of M_1/FeO_x.

Compared to the calculated activation energy barriers for CO + O_B → CO_2 through the L–H mechanism, the barrier with the E–R mechanism is much higher on these SACs. Consequently, the formation of the first CO_2 most likely occurs through the L–H mechanism on these M_1/FeO_x SACs (M = Fe, Co; Ru, Rh; Os, Ir).

3.1.2 *Formation of the first CO_2 with activated molecular oxygen*

In addition to the aforementioned dissociation adsorption pattern on FeO_x, gaseous O_2 can be well activated through the formation of O_2^- superoxide adsorbate on the surfaces of M_1/FeO_x (M = Pt, Au, Ni) when electron transfer is possible. Such an activation pattern of O_2 is also found on other M_1/FeO_x (M = Cu, Pd, and Ag) SACs, which is consistent with the results of a previous study [61] on Cu_1/FeO_x and Pd_1/FeO_x. In order to compare the energy profiles over these M_1/FeO_x (M = Ni, Cu; Pd, Ag; Pt, Au) catalysts, we collected the data of the proposed reaction pathways in Fig. 2 and Table S3 (in the ESM); the general schematic drawings of the corresponding optimized structures in each step are shown beneath the reaction pathways in Fig. 2. The optimized partial bond lengths of these SACs are shown in Table S4 (in the ESM).

Figure 2 and Table S4 (in the ESM) show that the O_{vac} on the O_3-terminated Fe_2O_3 (0001) surface (step i) serves as the anchoring site for the molecular adsorption of O_2 in step ii_{ad}. Accordingly, the adsorbed O_2 is

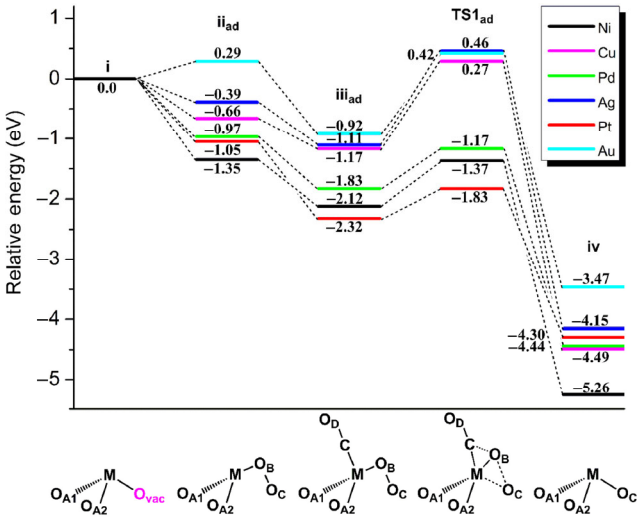

Figure 2 Proposed reaction pathway with oxygen absorption for the formation of the first CO_2 on the M_1/FeO_x (M = Ni, Cu, Pd, Ag, Pt, Au) catalysts, starting from the surface with an O_{vac}. The schematic structures of the supported single metal atoms shown at the bottom correspond to the structures at each step.

activated by the single atoms and the adjacent O_{vac} to form adsorbed O_2^- anion, and the O_B–O_C bond is elongated from 1.22 to 1.34 Å for Cu_1/FeO_x, to 1.39 Å for Pd_1/FeO_x, and to 1.35 Å for Ag_1/FeO_x; these O_B–O_C bond lengths are similar to those previously reported for Au_1/FeO_x and Ni_1/FeO_x of 1.37 and 1.35 Å, respectively, but shorter than that for Pt_1/FeO_x (1.46 Å).

Next, a CO molecule in the gas phase can be adsorbed on single Ni, Cu, Pd, Ag, Pt, and Au atoms (step iii_{ad}), and the calculated CO adsorption energies were 0.77, 0.51, 0.86, 0.72, 1.27, and 1.21 eV, respectively. With the adsorbed CO molecule (CO_{ad}) and O_B atom from activated O_2 close to each other, the first CO_2 molecule is generated (CO_{ad} + O_B → CO_2, $TS1_{ad}$); the C–O_B distances are shortened from 2.87 to 2.07 Å (Ni), 2.92 to 2.25 Å (Cu), 2.80 to 1.92 Å (Pd), 3.36 to 2.44 Å (Ag), 2.75 to 2.66 Å (Pt), and 3.54 to 2.02 Å (Au), leading to activation barriers of 0.75, 1.44, 0.66, 1.57, 0.49, and 1.34 eV on M_1/FeO_x when M is Ni, Cu, Pd, Ag, Pt, and Au, respectively.

The activation barriers of 0.49, 0.75, and 0.66 eV with Pt_1/FeO_x, Ni_1/FeO_x, and Pd_1/FeO_x, respectively, are low enough to allow the reaction to occur at a low temperature, while the high barriers of 1.44, 1.57, and 1.34 eV with Cu_1/FeO_x, Ag_1/FeO_x, and Au_1/FeO_x, respectively, indicate that the reaction is only possible

at high temperatures. Once the reaction passes $TS1_{ad}$, the first CO_2 is released from the surfaces of M_1/FeO_x (M = Ni, Cu; Pd, Ag; Pt, Au) and the O_C atom remains to restore the stoichiometric hematite surface (step iv).

3.1.3 *Formation of the second CO_2 on M_1/FeO_x*

The proposed reaction pathways for the formation of the second CO_2 on the M_1/FeO_x SACs are shown in Figs. 3 and 4, with the optimized partial bond lengths shown in Tables S5 and S6 (in the ESM). Figures 3 and 4 show that, on the single-M_1-atom-substituted stoichiometric hematite surfaces (step iv), the adsorption of a second CO molecule occurs (step v), and this CO molecule can approach the nearby lattice oxygen atoms on the surface, i.e., O_C at O_{vac}. However, different reaction pathways can be involved for different metals on FeO_x. M_1/FeO_x SACs containing Fe, Co, Rh, Pd, or Au prefer reaction pathway I, those containing Pt or Ir prefer pathway II, and those containing Ni, Cu, Ru, Ag, or Os prefer pathway III.

In pathway I, $CO_{ad} + O_C \rightarrow CO_2$ via the L–H mechanism occurs on the surfaces of M_1/FeO_x SACs containing Fe, Co, Rh, Pd, and Au with activation barriers of 0.66, 0.63, 1.05, 0.52, and 0.84 eV (TS2), respectively. As the reaction passes TS2, the as-formed CO_2 molecules are still adsorbed on the surfaces (step vi). Desorption of this CO_2 has energy barriers of 1.09, 1.16, 0.63, 0.21, and 0.80 eV (TS3) with Fe, Co, Rh, Pd, and Au SACs, respectively. In pathway II, the adsorbed CO gradually approaches the O_C atom of the SACs through transition states with a small imaginary vibration frequency (TS2). Afterwards, the adsorbed CO molecule can react with the O_C atom (step vi), leading to the production of CO_2 with energy barriers of 1.40 and 0.79 eV (TS3) for Ir_1/FeO_x and Pt_1/FeO_x, respectively. We repeated our previous calculations [1] and found that there exists one transition state (TS2) between steps v and vi, where the adsorbed CO gradually approaches the O_C atom on the surface of Pt_1/FeO_x through TS2 with a small imaginary vibration frequency (112 cm^{-1}) over a low barrier (0.23 eV). For pathway III, as shown in Fig. 4, the adsorbed CO (step v) gradually approaches O_C at the O_{vac} and forms the second CO_2 (TS2) directly on M_1/FeO_x catalysts containing Ni, Cu, Ru, Ag, and Os, and $CO_{ad} + O_C \rightarrow CO_2$ occurs via the L–H mechanism with energy barriers of 0.64, 0.56, 1.40, 0.72, and 1.85 eV, respectively. Finally, after the second CO_2 is released,

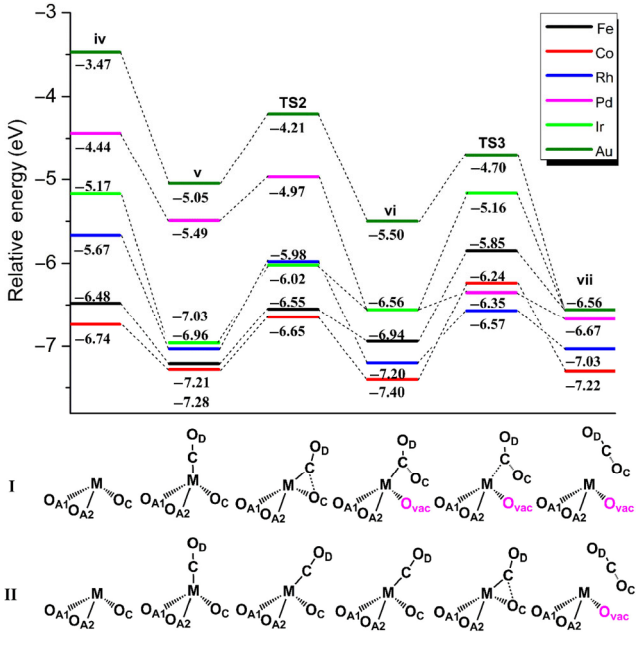

Figure 3 Proposed reaction pathways I and II for the formation of the second CO_2 on the M_1/FeO_x (M = Fe, Co; Rh, Pd; Ir, Au) catalysts, starting from a surface O_{vac}. The schematic structures of the supported single metal atoms shown at the bottom correspond to the structures at each step.

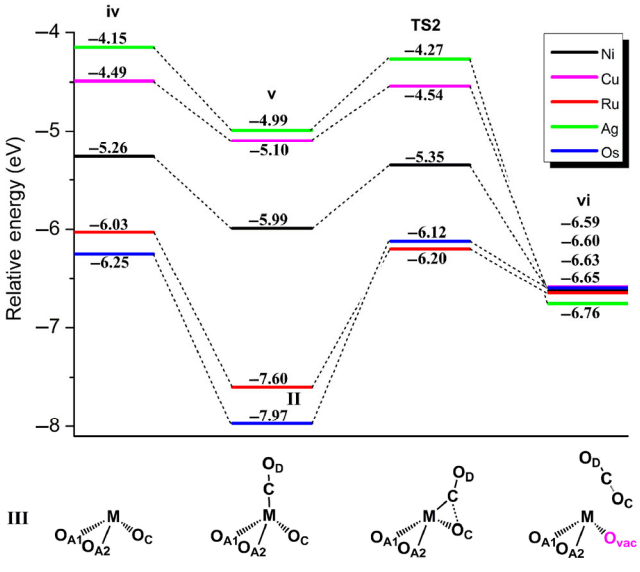

Figure 4 Proposed reaction pathway III for the formation of the second CO_2 on the M_1/FeO_x (M = Ni, Cu; Ru, Ag; Os) catalysts, starting from a surface without O_{vac}. The schematic structures of the supported single metal atoms shown at the bottom correspond to the structures at each step. See the caption of Fig. 1.

the stoichiometric hematite surface (step vii) of M_1/FeO_x is restored to that of the original catalyst with O_{vac} (step i). These steps thus complete the catalytic cycles. It is clear that the catalytic cycle can similarly start with the stoichiometric hematite surfaces (step vii) of M_1/FeO_x catalysts, leading to the generation of O_{vac} (step i) via the Mars–van Krevelen (MvK) mechanism.

3.2 Evaluation of CO oxidation activities of M_1/FeO_x catalysts

To systematically compare the catalytic activities of these SACs for CO oxidation, the activation barriers of the rate-determining step (RDS) were calculated, and they are shown in Fig. 5. As can be seen, the tendencies of the highest activation barriers for CO oxidation for each of these catalysts are similar across the periodic table for 3d, 4d, and 5d metals. The RDS activation barriers for M_1/FeO_x when M is Ni, Pd, and Pt in the catalytic cycles are less than 0.80 eV, indicating that CO_2 formation is fairly easy at room temperature when taking into account the contributions of enthalpy and entropy effects. In contrast, CO oxidation with the other FeO_x-based SACs have RDS energy barriers greater than 1.0 eV, suggesting that it only occurs at a relatively high temperature with these catalysts. In addition, the RDS is the formation of the first CO_2 when M is Cu, Ag, and Au and the formation of the second CO_2 when M is Fe, Ru, Rh, Os, and Ir, indicating that it is in fact metal-dependent even if similar reaction mechanisms are involved.

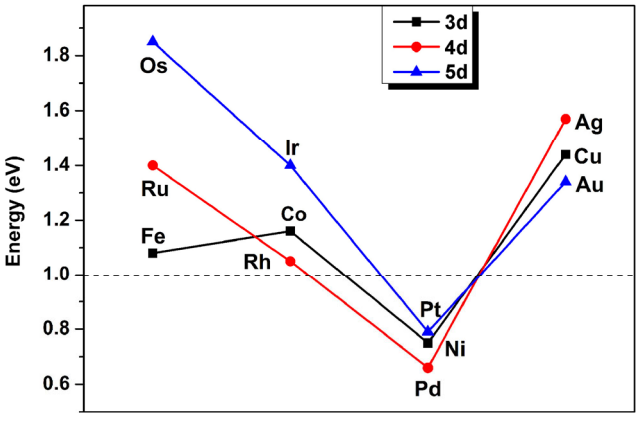

Figure 5 Calculated RDS activation energies for CO oxidation on the M_1/FeO_x (M = Fe, Co, Ni, Cu; Ru, Rh, Pd, Ag; Os, Ir, Pt, Au) SACs.

In general, the adsorption strength of CO on single atoms is an important factor in the catalytic activation by an SAC for CO oxidation, especially for the activation barrier of the formation of the second CO_2. For example, the calculated CO adsorption energies on a perfect surface of M_1/FeO_x SACs containing Ru, Rh, Os, and Ir are comparatively high, reaching up to 1.57, 1.36, 1.72, and 1.79 eV, respectively.

The higher adsorption energies lead to higher activation barriers (1.40, 1.05, 1.85, and 1.40 eV, respectively) for $CO_{ad} + O_{lattice} \rightarrow CO_2$. In contrast, M_1/FeO_x SACs containing Ni, Pd, and Pt lead to low activation barriers (0.64, 0.52, and 0.79 eV), corresponding to their lower CO adsorption energies (0.73, 1.05, and 1.08 eV). Here, it is interesting to note that the SACs with Ni, Pd, and Pt, which have ten valence electrons, exhibited the best catalytic performances in CO oxidation. To investigate further the interaction between single Ni, Pd, and Pt atoms and the adsorbed CO, the local density-of-states (LDOS) of Ni-3d (Pd-4d, Pt-5d) and C-2p (of adsorbed CO) orbitals were examined and are shown in Fig. 6. Clearly, the 3d (Ni) states are energetically close to the 2p (C) states of the adsorbed CO on the single Ni_1 atom near the Fermi level (E_F), suggesting that there is a relatively strong interaction between the single Ni_1 atom and the C atom of the adsorbed CO molecule. This mixture of the d states of the single metal atoms with the 2p (C) states was also observed on the single Pd_1 and Pt_1 atoms on FeO_x, indicative of strong CMSIs [57].

Our previous theoretical model successfully predicted the reactivity of Ir_1/FeO_x in CO oxidation. The activation barrier and CO adsorption energy were higher by 0.62 and 0.69 eV, respectively, than those with the Pt_1/FeO_x catalyst [1], indicating that Ir_1/FeO_x should be less active. Indeed, our experiment revealed that the Ir_1/FeO_x catalyst was less active for CO oxidation than Pt_1/FeO_x was, consistent with the theoretical prediction. Based on the current results, a new promising FeO_x-based catalyst, Pd_1/FeO_x, is predicted to show excellent activity in CO oxidation, even better than those of the previously reported Pt_1/FeO_x and Ni_1/FeO_x SACs [1, 59].

Interestingly, the RDS with Co_1/FeO_x and Fe_1/FeO_x is the TS3 step for the desorption of the second CO_2 through the bent CO_2 molecules (vi) on the surface.

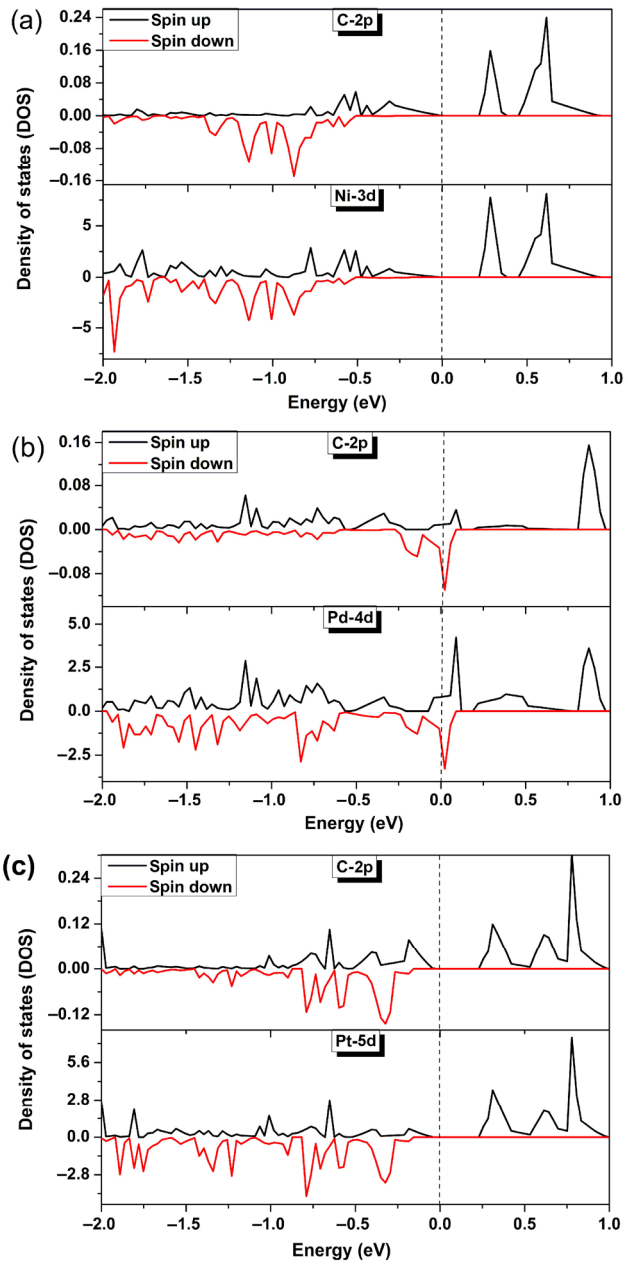

Figure 6 Spin-polarized LDOS projected on (a) Ni-3d, (b) Pd-4d, (c) Pt-5d, and C-2p (of adsorbed CO) orbitals. The Fermi level was set at zero.

The angles of these bent CO_2 molecules were 138.7° and 145.1°, which are similar to that of the CO_2^- anion in a previous study [85]. Presumably, the bent CO_2^- can lose one electron, leading to the formation of a linear CO_2 molecule [86], which desorbs from the surfaces of Co_1/FeO_x and Fe_1/FeO_x. The calculated adsorption energies of bent CO_2^- on the surface of Co_1/FeO_x and Fe_1/FeO_x were −0.89 and −0.44 eV. Thus, the activation energies of 1.16 and 1.09 eV are slightly high for the formation of the second CO_2.

The d-band centers of single M_1 atoms in M_1/FeO_x can also be used as overall evaluation parameters for the activities of these catalysts for CO oxidation because CO adsorption on M_1 depends on the metal-adsorbate binding strength, which is related to the $5\sigma \rightarrow$ d donation interaction and d $\rightarrow 2\pi$ back-donation interaction between the d-band and the adsorbate. When the d-band is too high or too low, it cannot match the energy levels of CO. The calculated d-band centers are shown in Fig. 7 for single metal atoms in M_1/FeO_x SACs with (i) and without an oxygen vacancy (iv). It is interesting to note that the energy curves cross in an area of the d-band centers of Ni, Pd, and Pt in M_1/FeO_x SACs. Overall, with (i) and without an oxygen vacancy (iv), the d-band centers of the M_1/FeO_x catalysts with Ni, Pd, and Pt lie in the middle, while those of the SACs with other metals are either too high or too low. Thus, it is not surprising that the Ni, Pd, and Pt SACs show the best overall catalytic performances for CO oxidation among SACs with group VIII to group IB elements (Fig. 5). This result indicates that the d-band centers of the single M_1 atoms (M = Fe, Co, Ni, Cu; Ru, Rh, Pd, Ag; Os, Ir, Pt, Au) in M_1/FeO_x SACs could be used to determine whether the energy match between SACs and adsorbed small molecules is appropriate, even though they depend on diverse chemical interactions between the different single metal atoms and the FeO_x support and adsorbates.

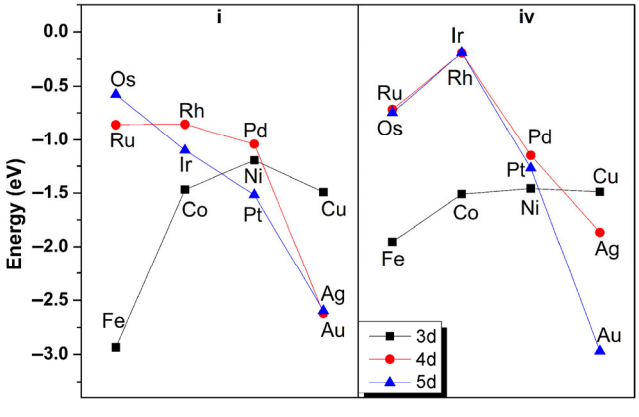

Figure 7 d-Band centers of M_1 (M = Fe, Co, Ni, Cu; Ru, Rh, Pd, Ag; Os, Ir, Pt, Au) in M_1/FeO_x SACs with (i) and without an oxygen vacancy (iv).

3.3 Oxidation states of single M_1 atoms in M_1/FeO_x

The oxidation state (OS) of an element in an active center and support is central to metal-based catalysis, especially when redox processes are involved [29]. To determine the possible oxidation states of single metal atoms in M_1/FeO_x with (i) and without an oxygen vacancy (iv) during the catalytic cycles, we proposed a scheme to estimate the OS of the single metal atoms supported on or embedded in the surface [1]. By calculating the charges of the surface-supported single atoms with selected model clusters, one can estimate the OS. Bader charges [87] of these single M_1 atoms were calculated and analyzed. For comparison [57], we also calculated the Bader charges of Co, Cu, Ru, Rh, Pd, Ag, and Os in $M(OH)_x$ (x = 1–4) models with oxidation states of I to IV in a 20 Å × 20 Å × 20 Å cubic box as rough criteria. The calculated Bader charges of these species are listed in Tables S7–S9 in the ESM. The results show that the single Fe, Ni, Cu, Rh, Ag, Os, and Ir atoms in M_1/FeO_x with an O vacancy have oxidation states close to II, while Fe, Co, Cu, Ru, Rh, Pd, and Os in M_1/FeO_x without an O vacancy have oxidation states of approximately III. The single Co_1 atom in Co_1/FeO_x is very similar to Co(I), and Ru_1 and Pd_1 in Ru_1/FeO_x and Pd_1/FeO_x with an O vacancy have oxidation states between I and II. Without an O vacancy, the single Ni_1 and Ir_1 atoms in Ni_1/FeO_x and Ir_1/FeO_x have oxidation states between III and IV, while the oxidation state of the single Ag_1 atom in Ag_1/FeO_x seems to lie between II and III. The actual OSs of these single atoms are hard to determine experimentally because of the low percentage of these sites on the surfaces. As indicated by our previous calculations for Pt_1 and Au_1 on FeO_x [86], there is strong covalent M–O chemical bonding between these nonzero-valent single M_1 atoms and the O atoms on the supports owing to the electron transfer from M_1 to the surrounding O atoms on the support. This strong covalent and ionic interaction and the high-valent natures make the aggregation of these single metal atoms into nanoclusters on the surface of FeO_x difficult, which can explain the extremely high stability of M_1/FeO_x in CO oxidation.

4 Conclusions

In this study, extensive DFT calculations were used to examine the activities and catalytic mechanism of M_1/FeO_x SACs (M = Co, Cu; Ru, Rh, Pd, Ag; Os) in CO oxidation. By combining our present results with those of our previous investigations on M_1/FeO_x (M = Fe, Ni; Ir, Pt, Au), we were able to systematically compare the catalytic activities and mechanisms of FeO_x-supported 3d, 4d, and 5d metals from groups VIII to IB (Fe, Co, Ni, Cu; Ru, Rh, Pd, Ag; Os, Ir, Pt, Au). We found different catalytic mechanisms for the formation of the first CO_2 that were related to different adsorption states of O_2 on these SACs: the dissociation of oxygen on M_1/FeO_x when M is Fe, Co, Ru, Rh, Os, or Ir and the adsorption of O_2 on M_1/FeO_x when M is Ni, Cu, Pd, Ag, Pt, or Au. Moreover, we predicted three different catalytic pathways, I, II, and III, for the formation of the second CO_2 on these SACs.

Our calculated results indicated that the M_1/FeO_x SACs containing Fe, Co, Ru, Rh, Os, and Ir with the oxygen dissociation mechanism and those containing Ni, Pd, and Pt with the oxygen adsorption mechanism show high catalytic activity for the formation of the first CO_2 through the Langmuir–Hinshelwood mechanism. In contrast, the M_1/FeO_x SACs with Cu, Ag, and Au with the oxygen adsorption mechanism show relatively low catalytic activity for the formation of the first CO_2. In addition, the second CO_2 forms via the Langmuir–Hinshelwood mechanism on the surfaces of M_1/FeO_x containing Fe, Co, Rh, Pd, and Au through pathway I; M_1/FeO_x containing Pt and Ir through pathway II; and M_1/FeO_x containing Ni, Cu, Ru, Ag, and Os through pathway III.

Finally, we predicted that a new noble-metal SAC, Pd_1/FeO_x, will show high activity in CO oxidation at low temperatures and be even better than the previously reported Pt_1/FeO_x and Ni_1/FeO_x SACs. The systematic investigations revealed trends in the activities and stabilities of FeO_x-supported single atoms of 3d, 4d, and 5d metals from groups VIII to IB. These results will help in better understanding the fundamental mechanisms of interactions between an FeO_x substrate and atomically dispersed single metal

atoms and designing highly active FeO_x-supported SACs. For a given catalytic reaction, the general trends of SACs with different oxide supports can be evaluated in the same way. This approach can be used to screen various SACs and evaluate and optimize their catalytic performances.

Acknowledgements

We acknowledge simulating discussion with Professor Qingfeng Ge. This work was supported by the National Natural Science Foundation of China (Nos. 21590792, 91645203, and 21521091 to J. L.; 21503046 to J. X. L. and 21203182 to X. F. Y.), and National Basic Research Program of China (No. 2013CB834603 to J. L.), Natural Science Foundation of Guizhou Province of China (No. QKJ[2015]2122), Natural Science foundation of Department of Education of Guizhou Province (Nos. QJTD[2015]55 and ZDXK[2014]18) and the GZEU start up package. The calculations were done using supercomputers at Tsinghua National Laboratory for Information Science and Technology, the State Key Laboratory of Physical Chemistry of Solid Surfaces (Xiamen University), and Guizhou Provincial High-Performance Computing Center of Condensed Materials and Molecular Simulation. This project is partially supported by the Open Fund of Shaanxi Key Laboratory of Catalysis to J. X. L. (No. SXKLC-2017-01).

Electronic Supplementary Material: Supplementary material (calculated adsorption and dissociated energies of O_2 on O_{vac}, the relavant bond lengths of M_1/FeO_x, Bader charges for M_1 single atoms) is available in the online version of this article at https://doi.org/10.1007/s12274-017-1775-0.

References

[1] Qiao, B. T.; Wang, A. Q.; Yang, X. F.; Allard, L. F.; Jiang, Z.; Cui, Y. T.; Liu, J. Y.; Li, J.; Zhang, T. Single-atom catalysis of CO oxidation using Pt_1/FeO_x. *Nat. Chem.* **2011**, *3*, 634–641.

[2] Gómez-Cortés, A.; Díaz, G.; Zanella, R.; Ramírez, H.; Santiago, P.; Saniger, J. M. Au–Ir/TiO_2 Prepared by deposition precipitation with urea: Improved activity and stability in CO oxidation. *J. Phys. Chem. C* **2009**, *113*, 9710–9720.

[3] Huang, Y. Q.; Wang, A. Q.; Li, L.; Wang, X. D.; Su, D. S.; Zhang, T. "Ir-in-ceria": A highly selective catalyst for preferential CO oxidation. *J. Catal.* **2008**, *255*, 144–152.

[4] Wang, H. T.; Feng, Q.; Cheng, Y. C.; Yao, Y. B.; Wang, Q. X.; Li, K.; Schwingenschlögl, U.; Zhang, X. X.; Yang, W. Atomic bonding between metal and graphene. *J. Phys. Chem. C* **2013**, *117*, 4632–4638.

[5] Wang, Y. G.; Yoon, Y.; Glezakou, V. A.; Li, J.; Rousseau, R. The role of reducible oxide–metal cluster charge transfer in catalytic processes: New insights on the catalytic mechanism of CO oxidation on Au/TiO_2 from *ab initio* molecular dynamics. *J. Am. Chem. Soc.* **2013**, *135*, 10673–10683.

[6] Xu, B. Q.; Wei, J. M.; Yu, Y. T.; Li, Y.; Li, J. L.; Zhu, Q. M. Size limit of support particles in an oxide-supported metal catalyst: Nanocomposite Ni/ZrO_2 for utilization of natural gas. *J. Phys. Chem. B* **2003**, *107*, 5203–5207.

[7] Haruta, M. Size- and support-dependency in the catalysis of gold. *Catal. Today* **1997**, *36*, 153–166.

[8] Lin, J.; Wang, A. Q.; Qiao, B. T.; Liu, X. Y.; Yang, X. F.; Wang, X. D.; Liang, J. X.; Li, J.; Liu, J. Y.; Zhang, T. Remarkable performance of Ir_1/FeO_x single-atom catalyst in water gas shift reaction. *J. Am. Chem. Soc.* **2013**, *135*, 15314–15317.

[9] Liang, J. X.; Wang, Y. G.; Yang, X. F.; Xing, D. H.; Wang, A. Q.; Zhang, T.; Li, J. Recent advances in single-atom catalysis. In *Encyclopedia of Inorganic and Bioinorganic Chemistry*; Scott, R. A., Eds.; John Wiley & Sons, Inc.: London, 2017; pp 1–11.

[10] Yang, X. F.; Wang, A. Q.; Qiao, B. T.; Li, J.; Liu, J. Y.; Zhang, T. Single-atom catalysts: A new frontier in heterogeneous catalysis. *Acc. Chem. Res.* **2013**, *46*, 1740–1748.

[11] Guo, X. G.; Fang, G. Z.; Li, G.; Ma, H.; Fan, H. J.; Yu, L.; Ma, C.; Wu, X.; Deng, D. H.; Wei, M. M. et al. Direct, nonoxidative conversion of methane to ethylene, aromatics, and hydrogen. *Science* **2014**, *344*, 616–619.

[12] Lin, J.; Qiao, B. T.; Li, N.; Li, L.; Sun, X. C.; Liu, J. Y.; Wang, X. D.; Zhang, T. Little do more: A highly effective Pt_1/FeO_x single-atom catalyst for the reduction of NO by H_2. *Chem. Commun.* **2015**, *51*, 7911–7914.

[13] Hou, C.; Zhao, G. F.; Ji, Y. J.; Niu, Z. Q.; Wang, D. S.; Li, Y. D. Hydroformylation of alkenes over rhodium supported on the metal-organic framework ZIF-8. *Nano Res.* **2014**, *7*, 1364–1369.

[14] Wang, Y.; Chen, Z.; Shen, R. A.; Cao, X.; Chen, Y. G.; Chen, C.; Wang, D. S.; Peng, Q.; Li, Y. D. Pd-dispersed CuS hetero-nanoplates for selective hydrogenation of phenylacetylene. *Nano Res.* **2016**, *9*, 1209–1219.

[15] Huang, Z. W.; Gu, X.; Cao, Q. Q.; Hu, P. P.; Hao, J. M.; Li, J. H.; Tang, X. F. Catalytically active single-atom sites fabricated from silver particles. *Angew. Chem., Int. Ed.* **2012**, *124*, 4274–4279.

[16] Wang, L.; Zhang, S. R.; Zhu, Y.; Patlolla, A.; Shan, J. J.; Yoshida, H.; Takeda, S.; Frenkel, A. I.; Tao, F. Catalysis and *in situ* studies of Rh_1/Co_3O_4 nanorods in reduction of NO with H_2. *ACS Catal.* **2013**, *3*, 1011–1019.

[17] Kwak, J. H.; Kovarik, L.; Szanyi, J. Heterogeneous catalysis on atomically dispersed supported metals: CO_2 reduction on multifunctional Pd catalysts. *ACS Catal.* **2013**, *3*, 2094–2100.

[18] Chu, M. W.; Chen, C. H. Chemical mapping and quantification at the atomic scale by scanning transmission electron microscopy. *ACS Nano* **2013**, *7*, 4700–4707.

[19] Lin, S.; Ye, X. X.; Johnson, R. S.; Guo, H. First-principles investigations of metal (Cu, Ag, Au, Pt, Rh, Pd, Fe, Co, and Ir) doped hexagonal boron nitride nanosheets: Stability and catalysis of CO oxidation. *J. Phys. Chem. C* **2013**, *117*, 17319–17326.

[20] Sun, S. H.; Zhang, G. X.; Gauquelin, N.; Chen, N.; Zhou, J. G.; Yang, S. L.; Chen, W. F.; Meng, X. B.; Geng, D. S.; Banis, M. N. et al. Single-atom catalysis using Pt/graphene achieved through atomic layer deposition. *Sci. Rep.* **2013**, *3*, 1775.

[21] Moses-DeBusk, M.; Yoon, M.; Allard, L. F.; Mullins, D. R.; Wu, Z. L.; Yang, X. F.; Veith, G.; Stocks, G. M.; Narula, C. K. CO oxidation on supported single Pt atoms: Experimental and *ab initio* density functional studies of CO interaction with Pt atom on θ-Al_2O_3(010) surface. *J. Am. Chem. Soc.* **2013**, *135*, 12634–12645.

[22] Guo, Z.; Liu, B.; Zhang, Q. H.; Deng, W. P.; Wang, Y.; Yang, Y. H. Recent advances in heterogeneous selective oxidation catalysis for sustainable chemistry. *Chem. Soc. Rev.* **2014**, *43*, 3480–3524.

[23] Xing, J.; Chen, J. F.; Li, Y. H.; Yuan, W. T.; Zhou, Y.; Zheng, L. R.; Wang, H. F.; Hu, P.; Wang, Y.; Zhao, H. J. et al. Stable isolated metal atoms as active sites for photocatalytic hydrogen evolution. *Chem.—Eur. J.* **2014**, *20*, 2138–2144.

[24] Flytzani-Stephanopoulos, M. Gold atoms stabilized on various supports catalyze the water–gas shift reaction. *Acc. Chem. Res.* **2014**, *47*, 783–792.

[25] Long, B.; Tang, Y.; Li, J. New mechanistic pathways for CO oxidation catalyzed by single-atom catalysts: Supported and doped Au_1/ThO_2. *Nano Res.* **2016**, *9*, 3868–3880.

[26] Liang, J. X.; Yang, X. F.; Xu, C. Q.; Zhang, T.; Li, J. On the catalytic activities of single-atom catalysts for CO oxidation: Pt_1/FeO_x vs. Fe_1/FeO_x. *Chin. J. Catal.*, in press, DOI: 10.1016/S1872-2067(17)62879-1.

[27] Nie, G. Y.; Li, P.; Liang, J. X.; Zhu, C. Theoretical investigation on the photocatalytic activity of the Au/g-C_3N_4 monolayer. *J. Theor. Comput. Chem.* **2017**, *16*, 1750013.

[28] Liu, J. C.; Wang, Y. G.; Li, J. Toward rational design of oxide-supported single-atom catalysts: Atomic dispersion of gold on ceria. *J. Am. Chem. Soc.* **2017**, *139*, 6190–6199.

[29] Tang, Y.; Zhao, S.; Long, B.; Liu, J. C.; Li, J. On the nature of support effects of metal dioxides MO_2 (M = Ti, Zr, Hf, Ce, Th) in single-atom gold catalysts: Importance of quantum primogenic effect. *J. Phys. Chem. C* **2016**, *120*, 17514–17526.

[30] Wang, Y. G.; Mei, D. H.; Glezakou, V. A.; Li, J.; Rousseau, R. Dynamic formation of single-atom catalytic active sites on ceria-supported gold nanoparticles. *Nat. Commun.* **2015**, *6*, 6511.

[31] Zhang, S. R.; Nguyen, L.; Liang, J. X.; Shan, J. J.; Liu, J. Y.; Frenkel, A. I.; Patlolla, A.; Huang, W. X.; Li, J.; Tao, F. Catalysis on singly dispersed bimetallic sites. *Nat. Commun.* **2015**, *6*, 7938.

[32] Wei, H. S.; Liu, X. Y.; Wang, A. Q.; Zhang, L. L.; Qiao, B. T.; Yang, X. F.; Huang, Y. Q.; Miao, S.; Liu, J. Y.; Zhang, T. FeO_x-supported platinum single-atom and pseudo-single-atom catalysts for chemoselective hydrogenation of functionalized nitroarenes. *Nat. Commun.* **2014**, *5*, 5634.

[33] Fei, H. L.; Dong, J. C.; Arellano-Jiménez, M. J.; Ye, G. L.; Kim, N. D.; Samuel, E. L. G.; Peng, Z. W.; Zhu, Z.; Qin, F.; Bao, J. M. et al. Atomic cobalt on nitrogen-doped graphene for hydrogen generation. *Nat. Commun.* **2015**, *6*, 8668.

[34] Lin, F. H.; Chen, W.; Liao, Y. H.; Doong, R. A.; Li, Y. D. Effective approach for the synthesis of monodisperse magnetic nanocrystals and M-Fe_3O_4 (M = Ag, Au, Pt, Pd) heterostructures. *Nano Res.* **2011**, *4*, 1223–1232.

[35] Li, Z. Y.; Yuan, Z.; Li, X. N.; Zhao, Y. X.; He, S. G. CO oxidation catalyzed by single gold atoms supported on aluminum oxide clusters. *J. Am. Chem. Soc.* **2014**, *136*, 14307–14313.

[36] Liu, P. X.; Zhao, Y.; Qin, R. X.; Mo, S. G.; Chen, G. X.; Gu, L.; Chevrier, D. M.; Zhang, P.; Guo, Q.; Zang, D. D. et al. Photochemical route for synthesizing atomically dispersed palladium catalysts. *Science* **2016**, *352*, 797–800.

[37] Yang, S.; Tak, Y. J.; Kim, J.; Soon, A.; Lee, H. Support effects in single-atom platinum catalysts for electrochemical oxygen reduction. *ACS Catal.* **2017**, *7*, 1301–1307.

[38] Zhang, T. A new photochemical synthesis strategy for monoatomic palladium catalyst. *Acta Phys. Chim. Sin.* **2016**, *32*, 1551–1552.

[39] Guan, H. L.; Lin, J.; Qiao, B. T.; Miao, S.; Wang, A. Q.; Wang, X. D.; Zhang, T. Enhanced performance of Rh_1/TiO_2 catalyst without methanation in water-gas shift reaction. *AlChE J.* **2017**, *63*, 2081–2088.

[40] Cheng, N. C.; Stambula, S.; Wang, D.; Banis, M. N.; Liu, J.; Riese, A.; Xiao, B. W.; Li, R. Y.; Sham, T. K.; Liu, L. M. et al. Platinum single-atom and cluster catalysis of the hydrogen evolution reaction. *Nat. Commun.* **2016**, *7*, 13638.

[41] Xu, G.; Wei, H. S.; Ren, Y. J.; Yin, J. Z.; Wang, A. Q.; Zhang, T. Chemoselective hydrogenation of 3-nitrostyrene over a Pt/FeO_x pseudo-single-atom-catalyst in CO_2-expanded liquids. *Green Chem.* **2016**, *18*, 1332–1338.

[42] Wang, C. L.; Gu, X. K.; Yan, H.; Lin, Y.; Li, J. J.; Liu, D. D.; Li, W. X.; Lu, J. L. Water-mediated mars–van krevelen mechanism for CO oxidation on ceria-supported single-atom Pt_1 catalyst. *ACS Catal.* **2017**, *7*, 887–891.

[43] Yang, T.; Fukuda, R.; Hosokawa, S.; Tanaka, T.; Sakaki, S.; Ehara, M. A Theoretical investigation on CO oxidation by single-atom catalysts M_1/γ-Al_2O_3 (M = Pd, Fe, Co, and Ni). *ChemCatChem* **2017**, *9*, 1222–1229.

[44] Liu, J. Y. Catalysis by supported single metal atoms. *ACS Catal.* **2017**, *7*, 34–59.

[45] Tang, Y.; Wang, Y. G.; Liang, J. X.; Li, J. A DFT+U study of water adsorption and dissociation on Au_1/CeO_2 single-atom catalyst (SAC). *Chin. J. Catal.* **2017**, *38*, doi: 10.1016/S1872-2067(17)62829-8.

[46] Liu, Q. F.; Liu, Y.; Li, H. B.; Li, L. L.; Deng, D. H.; Yang, F.; Bao, X. H. Towards the atomic-scale characterization of isolated iron sites confined in a nitrogen-doped graphene matrix. *Appl. Surf. Sci.* **2017**, *410*, 111–116.

[47] Cao, X. R. Insight into mechanism and selectivity of propane dehydrogenation over the Pd-doped Cu(111) surface. *RSC Adv.* **2016**, *6*, 65524–65532.

[48] Li, C. Single Co atom catalyst stabilized in C/N containing matrix. *Chin. J. Catal.* **2016**, *37*, 1443–1445.

[49] Zhang, H. B.; Wei, J.; Dong, J. C.; Liu, G. G.; Shi, L.; An, P. F.; Zhao, G. X.; Kong, J. T.; Wang, X. J.; Meng, X. G. et al. Efficient visible-light-driven carbon dioxide reduction by a single-atom implanted metal–organic framework. *Angew. Chem., Int. Ed.* **2016**, *128*, 14522–14526.

[50] Kyriakou, G.; Boucher, M. B.; Jewell, A. D.; Lewis, E. A.; Lawton, T. J.; Baber, A. E.; Tierney, H. L.; Flytzani-Stephanopoulos, M.; Sykes, E. C. H. Isolated metal atom geometries as a strategy for selective heterogeneous hydrogenations. *Science* **2012**, *335*, 1209–1212.

[51] Liu, J. L.; Lucci, F. R.; Yang, M.; Lee, S.; Marcinkowski, M. D.; Therrien, A. J.; Williams, C. T.; Sykes, E. C. H.; Flytzani-Stephanopoulos, M. Tackling CO poisoning with single-atom alloy catalysts. *J. Am. Chem. Soc.* **2016**, *138*, 6396–6399.

[52] Huang, X. H.; Xia, Y. J.; Cao, Y. J.; Zheng, X. S.; Pan, H. B.; Zhu, J. F.; Ma, C.; Wang, H. W.; Li, J. J.; You, R. et al. Enhancing both selectivity and coking-resistance of a single-atom Pd_1/C_3N_4 catalyst for acetylene hydrogenation. *Nano Res.* **2017**, *10*, 1302–1312.

[53] Wang, C. Y.; Garbarino, G.; Allard, L. F.; Wilson, F.; Busca, G.; Flytzani-Stephanopoulos, M. Low-temperature dehydrogenation of ethanol on atomically dispersed gold supported on $ZnZrO_x$. *ACS Catal.* **2016**, *6*, 210–218.

[54] Yin, P. Q.; Yao, T.; Wu, Y.; Zheng, L. R.; Lin, Y.; Liu, W.; Ju, H. X.; Zhu, J. F.; Hong, X.; Deng, Z. X. et al. Single cobalt atoms with precise N-coordination as superior oxygen reduction reaction catalysts. *Angew. Chem., Int. Ed.* **2016**, *55*, 10800–10805.

[55] Zhu, C. Z.; Fu, S. F.; Shi, Q. R.; Du, D.; Lin, Y. H. Single-atom electrocatalysts. *Angew. Chem., Int. Ed.*, in press, DOI: 10.1002/anie.201703864.

[56] Liang, J. X.; Lin, J.; Yang, X. F.; Wang, A. Q.; Qiao, B. T.; Liu, J. Y.; Zhang, T.; Li, J. Theoretical and experimental investigations on single-atom catalysis: Ir_1/FeO_x for CO oxidation. *J. Phys. Chem. C* **2014**, *118*, 21945–21951.

[57] Qiao, B. T.; Liang, J. X.; Wang, A. Q.; Xu, C. Q.; Li, J.; Zhang, T.; Liu, J. J. Ultrastable single-atom gold catalysts with strong covalent metal-support interaction (CMSI). *Nano Res.* **2015**, *8*, 2913–2924.

[58] Qiao, B. T.; Liang, J. X.; Wang, A. Q.; Liu, J. Y.; Zhang, T. Single atom gold catalysts for low-temperature CO oxidation. *Chin. J. Catal.* **2016**, *37*, 1580–1586.

[59] Liang, J. X.; Yang, X. F.; Wang, A. Q.; Zhang, T.; Li, J. Theoretical investigations of non-noble metal single-atom catalysis: Ni_1/FeO_x for CO oxidation. *Catal. Sci. Technol.* **2016**, *6*, 6886–6892.

[60] Li, F. Y.; Li, Y. F.; Zeng, X. C.; Chen, Z. F. Exploration of high-performance single-atom catalysts on support M_1/FeO_x for CO oxidation via computational study. *ACS Catal.* **2015**, *5*, 544–552.

[61] Zhang, T. Theoretical design of oxide-supported single atom catalysts. *Acta Phys. Chim. Sin.* **2017**, *33*, 1–9.

[62] Gardner, S. D.; Hoflund, G. B.; Upchurch, B. T.; Schryer, D. R.; Kielin, E. J.; Schryer, J. Comparison of the performance characteristics of Pt/SnO_x and Au/MnO_x catalysts for low-temperature CO oxidation. *J. Catal.* **1991**, *129*, 114–120.

[63] Liu, J. F.; Chen, W.; Liu, X. W.; Zhou, K. B.; Li, Y. D. Au/$LaVO_4$ nanocomposite: Preparation, characterization, and catalytic activity for CO oxidation. *Nano Res.* **2008**, *1*, 46–55.

[64] Hu, L. H.; Sun, K. Q.; Peng, Q.; Xu, B. Q.; Li, Y. D. Surface active sites on Co_3O_4 nanobelt and nanocube model catalysts for CO oxidation. *Nano Res.* **2010**, *3*, 363–368.

[65] Chen, S. F.; Li, J. P.; Qian, K.; Xu, W. P.; Lu, Y.; Huang, W. X.; Yu, S. H. Large scale photochemical synthesis of

M@TiO_2 nanocomposites (M = Ag, Pd, Au, Pt) and their optical properties, CO oxidation performance, and antibacterial effect. *Nano Res*. **2010**, *3*, 244–255.

[66] Lin, J.; Wang, X. D.; Zhang, T. Recent progress in CO oxidation over Pt-group-metal catalysts at low temperatures. *Chin*. *J*. *Catal*. **2016**, *37*, 1805–1813.

[67] Wang, Y. G.; Yang, X. F.; Li, J. Theoretical studies of CO oxidation with lattice oxygen on Co_3O_4 surfaces. *Chin*. *J*. *Catal*. **2016**, *37*, 193–198.

[68] Wu, B. H.; Zhang, H.; Chen, C.; Lin, S. C.; Zheng, N. F. Interfacial activation of catalytically inert Au (6.7 nm)-Fe_3O_4 dumbbell nanoparticles for CO oxidation. *Nano Res*. **2009**, *2*, 975–983.

[69] Gokhale, A. A.; Dumesic, J. A.; Mavrikakis, M. On the mechanism of low-temperature water gas shift reaction on copper. *J*. *Am*. *Chem*. *Soc*. **2008**, *130*, 1402–1414.

[70] Fu, Q.; Saltsburg, H.; Flytzani-Stephanopoulos, M. Active nonmetallic Au and Pt species on ceria-based water-gas shift catalysts. *Science* **2003**, *301*, 935–938.

[71] Song, C. S. Fuel processing for low-temperature and high-temperature fuel cells: Challenges, and opportunities for sustainable development in the 21st century. *Catal*. *Today* **2002**, *77*, 17–49.

[72] Abbet, S.; Heiz, U.; Häkkinen, H.; Landman, U. CO oxidation on a single Pd atom supported on magnesia. *Phys*. *Rev*. *Lett*. **2001**, *86*, 5950–5953.

[73] Okumura, M.; Masuyama, N.; Konishi, E.; Ichikawa, S.; Akita, T. CO oxidation below room temperature over Ir/TiO_2 catalyst prepared by deposition precipitation method. *J*. *Catal*. **2002**, *208*, 485–489.

[74] Wang, Y. G.; Mei, D. H.; Li, J.; Rousseau, R. A DFT+U study on the localized electronic states and their potential role during H_2O dissociation and CO oxidation processes on CeO_2(111) surface. *J*. *Phys*. *Chem*. *C* **2013**, *117*, 23082–23089.

[75] Sandratskii, L. M.; Uhl, M.; Kübler, J. Band theory for electronic and magnetic properties of a-Fe_2O_3. *J*. *Phys*. *Condens*. *Matter* **1996**, *8*, 983–989.

[76] Wang, X. G.; Weiss, W.; Shaikhutdinov, S. K.; Ritter, M.; Petersen, M.; Wagner, F.; Schlögl, R.; Scheffler, M. The hematite (α-Fe_2O_3) (0001) surface: Evidence for domains of distinct chemistry. *Phys*. *Rev*. *Lett*. **1998**, *81*, 1038–1041.

[77] Kresse, G.; Hafner, J. *Ab initio* molecular dynamics for liquid metals. *Phys*. *Rev*. *B* **1993**, *47*, 558–561.

[78] Kresse, G.; Joubert, D. From ultrasoft pseudopotentials to the projector augmented-wave method. *Phys*. *Rev*. *B* **1999**, *59*, 1758–1775.

[79] Blöchl, P. E. Projector augmented-wave method. *Phys*. *Rev*. *B* **1994**, *50*, 17953–17979.

[80] Perdew, J. P.; Burke, K.; Ernzerhof, M. Generalized gradient approximation made simple. *Phys*. *Rev*. *Lett*. **1997**, *77*, 3865–3868.

[81] Dudarev, S. L.; Botton, G. A.; Savrasov, S. Y.; Szotek, Z.; Temmerman, W. M.; Sutton, A. P. Electronic structure and elastic properties of strongly correlated metal oxides from first principles: LSDA + U, SIC-LSDA and EELS study of UO_2 and NiO. *Phys*. *Stat*. *Sol*. *(A)* **1998**, *166*, 429–443.

[82] Henkelman, G.; Jónsson, H. A dimer method for finding saddle points on high dimensional potential surfaces using only first derivatives. *J*. *Chem*. *Phys*. **1999**, *111*, 7010–7022.

[83] Langmuir, I. The constitution and fundamental properties of solids and liquids. Part I. Solids. *J*. *Am*. *Chem*. *Soc*. **1916**, *38*, 2221–2295.

[84] Hinshelwood, C. N. *The Kinetics of Chemical Change*; Clarendon: Oxford, UK, 1940.

[85] Yoshioka, Y.; Schaefer III, H. F.; Jordan, K. D. Theoretical investigation of the electron affinity of CO_2. *J*. *Chem*. *Phys*. **1981**, *75*, 1040–1041.

[86] Pan, Y. X.; Liu, C. J.; Wiltowski, T. S.; Ge, Q. F. CO_2 adsorption and activation over γ-Al_2O_3-supported transition metal dimers: A density functional study. *Catal*. *Today* **2009**, *147*, 68–76.

[87] Tang, W.; Sanville, E.; Henkelman, G. A grid-based Bader analysis algorithm without lattice bias. *J*. *Phys*. *Condens*. *Matter* **2009**, *21*, 084204.